Research Article | Vol. 27, No. 20 | 30 Sep 2019 | OPTICS EXPRESS A1419
Optics EXPRESS

Energy yield analysis of textured perovskite silicon tandem solar cells and modules

N. Tucher,[1,2,*] O. Höhn,[1] J. N. Murthy,[1] J. C. Martinez,[1] M. Steiner,[1] A. Armbruster,[1] E. Lorenz,[1] B. Bläsi,[1] and J. C. Goldschmidt[1]

[1]*Fraunhofer Institute for Solar Energy Systems, ISE, Heidenhofstraße 2, 79100 Freiburg, Germany*
[2]*Albert-Ludwigs-University, Department of Sustainable Systems Engineering INATECH, Georges-Köhler-Allee 103, 79110 Freiburg, Germany*
**nico.tucher@ise.fraunhofer.de*

Abstract: Perovskite silicon tandem solar cells combine potentially low production costs with the ability to surpass the efficiency limit of silicon single junction solar cells. Optical modeling and optimization are crucial to achieve this ambitious goal in the near future. The optimization should seek to maximize the energy yield based on realistic environmental conditions. This work analyzes the energy yield of perovskite silicon tandem solar cells and modules based on realistic experimental data, with a special focus on the investigation of surface textures at the front and rear side of the solar cell and its implication for reflection as well as parasitic absorption properties. The investigation reveals a 7.3%$_{rel}$ higher energy yield for an encapsulated tandem cell with a textured front side compared with an encapsulated high efficiency single junction solar cell with 24.3% harvesting efficiency for irradiance data of the year 2014 in Freiburg/Germany.

1. Introduction

Based on the rapid development of hybrid organic-inorganic perovskites as solar cell absorber materials, perovskite silicon tandem solar cells have quickly reached the efficiency level of silicon single junction devices. The current record value of 28.0% for a two-terminal device [1] even overcame the silicon record of 26.7% [2]. Due to the much higher theoretical efficiency potential of tandem solar cells, significant further improvements are possible.

As perovskite silicon tandem solar cells are still in an early stage of development, a large variety of device configurations have been investigated over the last years. For a comparison of their performance the STC efficiency can be of limited value, because two-terminal tandem devices with the need for current-matching are more susceptible to environmental conditions that can vary strongly over the year or between different locations. The energy yield takes into account parameters like varying spectra, different angles of incidence or temperature. It is therefore a much more comprehensive figure of merit than the STC efficiency. Note that three- or four-terminal tandem devices might simplify the restrictions due to environmental conditions but increase complexity in the module fabrication process.

Purely theoretical analyses, e.g. based on the Shockley-Queisser-limit are helpful to understand the fundamental behavior and estimate the influence of environmental changes [3]. However, in order to derive specific recommendations for fabrication, realistic device configurations have to be investigated. For this task, optical and electrical device simulations are highly valuable.

The focus topics of most studies are the (i) module configuration, e.g. two-terminal vs. four-terminal, (ii) the material choice or (iii) the layer order and thicknesses in the perovskite top cell stack. Often a planar layer stack is optimized as top cell with regard to material properties and layer thicknesses, sometimes leading to predicted cell efficiencies above 30% [4–7].

#368615 https://doi.org/10.1364/OE.27.0A1419
Journal © 2019 Received 29 May 2019; revised 12 Jul 2019; accepted 12 Jul 2019; published 11 Sep 2019

Optics EXPRESS

Among the parameters, which are less often included in simulation studies are (iv) the integration of surface textures, (v) effects of the module encapsulation and (vi) a calculation of the energy yield including realistic environmental conditions as well as electrical properties.

An extensive study by Hörantner et al. optimized the layer thickness of planar perovskite silicon tandem devices considering the electrical properties of the device as well as measured irradiance data for different locations [4]. However, neither surface textures nor a module encapsulation were taken into account in this study. Jost et al. focus in their yield analysis on textured interfaces but take the full module stack with encapsulation only for some of the systems into account [8]. Jiang et al. investigate various tandem module configurations and point out the importance of the module encapsulation. However, no surface textures are included [9]. Van Eerden et al. investigate materials and include also surface roughness in a tandem device [10], but without calculating the energy yield.

Summarizing the available literature, a broad range of module configurations, material choices and layer stacks have been investigated. In some cases, surface textures, module encapsulation or an energy yield calculation were included. The only study available so far combining all aspects (i)-(vi) was performed by Lehr et al. [11].

In this work, we investigate the energy yield perovskite silicon two-terminal tandem modules, focusing on an optimization of the layer thickness, the introduction of surface textures and the calculation of the energy yield. In contrast to the work by Lehr et al. [11] an n-i-p configuration is investigated, with the electron contact layer deposited first on the silicon solar cell and the hole contact last on the sun-facing side. With this deposition sequence, the record efficiencies for single-junction perovskite solar cells have been achieved [12] and it is therefore an attractive system for further investigation. As we will see in the following, additional optical losses might occur in a tandem configuration. Therefore, further optimization is required, for which this paper presents a set of useful tools.

In sections 2 and 3 an overview of the investigated systems and an introduction to the simulation procedure in this work is given. Section 4 shows the simulation results and its implications for future development of perovskite silicon tandem modules.

2. Material choice and system configuration

The systems that are investigated within this work include realistic monolithic perovskite silicon tandem solar cells with textured front or rear side, a 250 µm thick silicon bulk and a silver rear reflector, without and with module encapsulation (see Fig. 1). The question whether systems with planar front side can perform similarly well as systems with textured front is highly relevant for further research as this can make a large difference for the applied deposition techniques.

The perovskite solar cell consists of a layer stack with indium tin oxide (ITO) [13] as charge transport material at the bottom and top, TiO_2 [14] and C60 [15] as electron contact materials, the perovskite absorber and Spiro-OMeTAD [16] as hole contact layer. The refractive index data of the perovskite absorber layer for different band gaps was adopted from [4]. The data for the silicon bulk was taken from [17] and for the silver reflector from [18]. The solar cells without encapsulation feature a magnesium fluoride (MgF_2) [19] top layer as anti-reflective coating (ARC). The module stack includes a 500 µm thick encapsulation made of ethyl vinyl acetate (EVA) using data from [20]. The module front features a planar ARC with a wavelength-independent refractive index of 1.27 and a thickness of 130 nm. Furthermore, a standard silicon solar cell with textured front and planar rear side and 70 nm thick silicon nitride ARC [21] is used as reference.

Optics EXPRESS

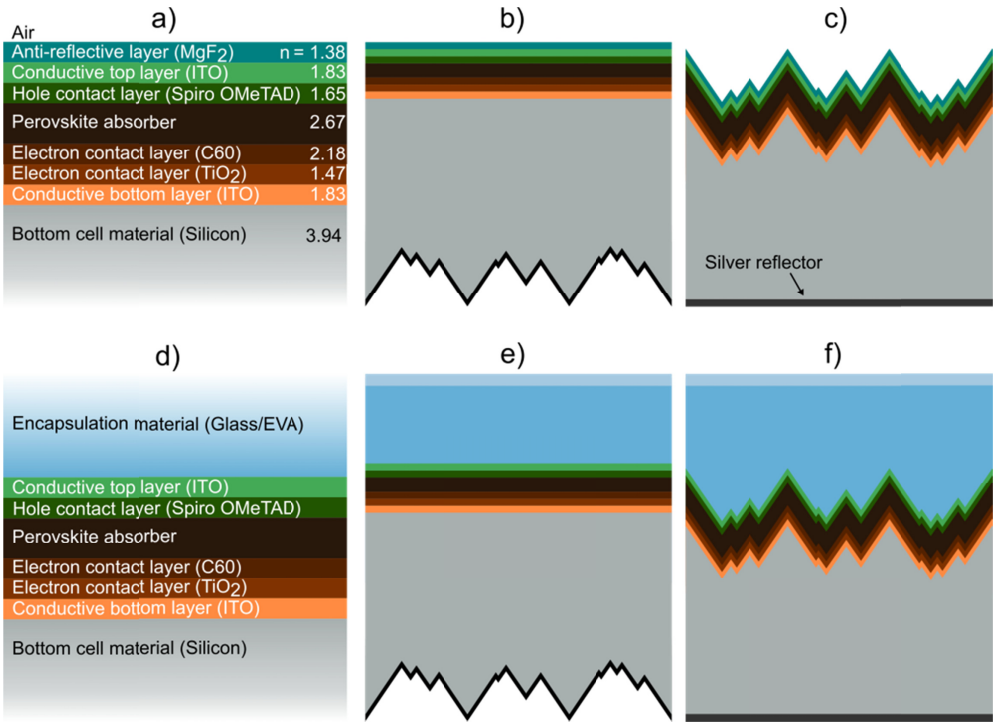

Fig. 1. Sketches of the perovskite silicon tandem solar cells and module stacks investigated in this work. a) Thin film stack of the perovskite top solar cell with refractive indices for a wavelength of 600 nm. b) Tandem cell with planar front side and random pyramid texture at the rear side as well as c) textured front side and planar rear side. d-f) similar configurations as described before, without MgF_2 anti-reflective coating but with module encapsulation and ARC at the module front side.

3. Summary of the modeling scheme

The yield analysis of solar modules with tandem solar cells is not straight forward. The following modeling scheme was applied for the simulations within this work. Details about the specific parameters are given in section 4.

i. Optimizing the perovskite solar cell

Starting point of the simulations is a layer thickness optimization of the perovskite cell, including the absorber itself as well as electron and hole transport layers. A thin film solver is used to model normal incidence on the device. The absorptance in the different layers as well as an approximative photocurrent density (J_{Ph}) in both subcells is calculated. Based on a genetic algorithm J_{Ph} is matched and maximized for a specific incidence direction and irradiance spectrum. More details of the procedure are described in [22].

ii. Calculating optical cell and module performance

The optical performance of both subcells is modeled with OPTOS (Optical Properties of Textured Optical Sheets), a matrix-based simulation formalism that focuses on solar cells with textured interfaces [22]. In order to perform OPTOS simulations for different arrangements, the light redistribution properties of all investigated surface textures are determined individually with the most appropriate method (transfer matrix formalism for planar interfaces and ray tracing for random pyramids). Subsequently, OPTOS is used to model the different configurations for a

large variety of incidence angles [23] covering the complete relevant angular space. This involves taking into account all the complex light paths and optical interactions between the interfaces.

iii. Collecting the time-resolved spectral irradiance

The wavelength and angular resolved spectral irradiance for different time steps can be modeled, e.g. by the widely used tool SMARTS2 [24], or it can be measured. While many works use a database provided by the National Renewable Energy Lab (NREL), this work is based on measured data from Freiburg, Germany.

iv. Determining electrical solar cell parameters

Among the different approaches to model the electrical solar cell performance, the application of a two-diode model for each of the subcells was chosen for this work. In spite of the simplicity of the model, it is able to describe the observed IV-characteristics well. The electrical parameters, which have to be determined for top and bottom cell, are the dark saturation currents (J_{01}, J_{02}) as well as parallel and series resistance (R_P, R_S).

v. Performing the yield analysis

The final yield calculation is based on the tool YieldOpt, which is an in-house development, described in [25] originally focusing on concentrating photovoltaics. YieldOpt 2.0 was extended with capabilities to include the varying angle of incidence of the solar radiation and the respective changes of the effective module area during the day and over the year. YieldOpt 2.0 combines all input parameters described above and determines the energy yield for the investigated period of time. An overview of the procedure is sketched in Fig. 2.

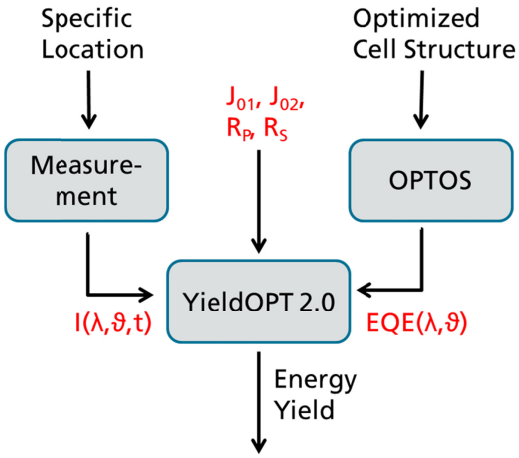

Fig. 2. Sketch summarizing the simulation procedure applied for the yield analysis of perovskite silicon tandem solar cells in this work.

4. Modeling details, results and discussion

4.1 Optimizing the performance perovskite solar cells for different band gaps

For the optimization of the perovskite solar cell stack the AM1.5g spectrum [26] and normal incidence were assumed. The refractive index data for the perovskite layer is based on measurements of MaPbI3 by Löper et al. [27] for a bandgap of 1.55 eV. In order to optimize the stack for different perovskite band gaps, the absorption coefficient $\alpha(\lambda)$ was shifted

Optics EXPRESS

along the energy axis as described in Hörantner et al., who calculated the imaginary part of the refractive via $k = \frac{\alpha \cdot \lambda}{4\pi}$ and subsequently retrieved the real part of the refractive index n using the Kramers-Kronig-relation [4].

The optimization of the layer thicknesses of the perovskite cell was performed as described in section 3 for bandgaps from 1.55 eV to 1.75 eV and the cell and module stack configurations depicted in section 2. The optimal layer thicknesses of top ITO, Spiro OMeTAD, C60, TiO_2 and bottom ITO converge during the optimization in all cases to their predefined minimum thicknesses of 60 nm, 50 nm, 10 nm, 10 nm and 20 nm respectively, due to the strong influence of their absorptivity. The optimized perovskite layer thicknesses are displayed in Table 1. Note that perovskite thicknesses above 2000 nm seem difficult to fabricate experimentally. Therefore, this value was set as maximum within this work. The ARC in the non-encapsulated case varies between 90 nm and 122 nm.

Table 1. Optimized thicknesses [nm] of the perovskite layer for different bandgaps, solar cell and module stack configuration

E_{Gap} [eV]	Perovskite layer thickness [nm]			
	Cell planar front	*Cell textured front*	*Module stack planar front*	*Module stack textured front*
1.55	313	305	317	287
1.60	428	398	411	373
1.65	597	591	597	549
1.70	1428	1477	1461	1290
1.75	2000	1996	2000	1994

4.2 Optical cell and module performance

The optical cell and module performance was determined using OPTOS simulations based on redistribution matrices for the optimized layer stacks and the silver rear reflector. Within each configuration and using the AM1.5g spectrum [26], similar matched photocurrent densities of the subcells were achieved for the different bandgaps, e.g. ranging from 17.7 mA/cm^2 to 17.8 mA/cm^2 for the module stack with planar front side. The only exception is the bandgap of 1.75 eV since the maximum perovskite layer thickness of 2000 nm is not large enough to reach current matching. In this case the top cell features a photocurrent of 16.7 mA/cm^2 while the bottom cell reaches 18.8 mA/cm^2, which will reduce the monolithic tandem cell performance. As the voltage increases with larger bandgaps, the bandgap of 1.70 eV is chosen for the following investigation.

A detailed optical loss analysis of the module configurations with planar and front side textured solar cells is shown in Fig. 3. This representation of the optical performance of the system reveals two main differences between both systems:

Integrating a pyramid texture at the front side of the silicon bottom cell reduces the direct reflection drastically, and the associated losses in photocurrent decrease from 4.8 mA/cm^2 to 0.8 mA/cm^2. The general effect is known from single junction silicon solar cells. However, the quantification for this realistic perovskite silicon tandem cell stack is a relevant step. Note that direct reflection means light that is reflected before entering the silicon solar cell, while escape reflectance means light that travelled at least once through the silicon solar cell, but then leaves the solar cell through the front surface.

The parasitic absorption in the charge carrier transport layers and transparent electrodes is already high for the planar front side, e.g. being equivalent to a loss in photocurrent of 1.8 mA/cm^2 in the top ITO. It increases even further for the textured front side to a value of 3.0

mA/cm^2. This is due to multiple interactions of the light with those layers within the pyramid interface.

The combination of all effects leads to a matched photocurrent density of 17.8 mA/cm^2 in the case with planar front side and 19.0 mA/cm^2 in the case with random pyramid front side demonstrating the superiority of the front side textured configuration.

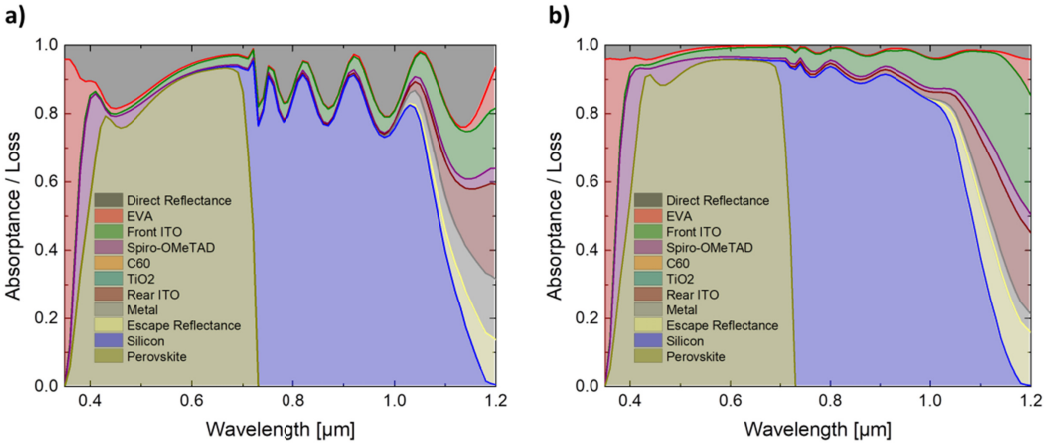

Fig. 3. Optical loss analysis of the two perovskite silicon tandem module stacks with planar front (left) and textured front (right). The texture reduces the front side reflectance considerably. Parasitic absorption in the Spiro-OMeTAD and the ITO layers is for both cases a relevant effect, even more pronounced in the case with front side texture.

The exact absorptance values for each layer are summarized in Table 2. Comparing those values to the study performed in [11] shows 1.1-1.3 mA/cm^2 lower current densities in the tandem cell. This is due to the different order of the layer stack with the Spiro layer on top of the perovskite and a resulting larger parasitic absorption.

Table 2. Absorbed or reflected photocurrent density [mA/cm^2]

	Module stack planar front	Module stack textured front
Direct reflectance	4.8	0.8
SiO_2	0.0	0.0
EVA	0.8	0.7
ITO	1.8	3.0
Spiro-OMEeTAD	0.8	1.2
Perovskite	**17.8**	**19.0**
C60	0.0	0.0
TiO_2	0.0	0.0
ITO	0.9	1.1
Silicon	**17.8**	**19.0**
Rear metal	0.7	0.3
Escape reflectance	0.5	0.9

Note, that parasitic absorption in the ITO strongly depends on the deposition technique and process parameters. The refractive index data that was used in this study describes an ITO that was not optimized to reach the highest transparency with just enough conductivity. Reducing the parasitic absorption in the ITO is therefore a highly relevant step for further improvements.

4.3 Time-resolved spectral irradiance

For the time-resolved spectral irradiance, measurement data from Freiburg, Germany, between February 2014 and January 2015 was used with a time resolution of one hour. The

spectral distribution of the global irradiance was measured using a spectrometer with south orientation and a tilt angle of 29°. Separate measurements of spectrally resolved diffuse and direct irradiance are not available. However, spectrally integrated diffuse and global horizontal irradiance, $I_{diffuse\text{-}horizontal}$ and $I_{global\text{-}horizontal}$, were measured at the same site. The direct and diffuse irradiance on the tilted module plane were calculated as follows:

(i) The direct part of the irradiance $I_{direct\text{-}horizontal}$ is calculated by subtracting $I_{diffuse\text{-}horizontal}$ from $I_{global\text{-}horizontal}$. Subsequently $I_{direct\text{-}horizontal}$ is converted to the $I_{direct\text{-}tilt}$, the direct irradiance incident on a plane with an orientation of 29° south taking into account the changing solar position.

(ii) The diffuse irradiance on a tilted plane consists of the sky-diffuse and the ground-reflected component.

$$I_{diffuse-tilt} = I_{sky-diffuse-tilt} + I_{ground-reflected} \quad (1)$$

The sky-diffuse part ist calculated based on the measured diffuse horizontal irradiance $I_{diffuse\text{-}horizontal}$ and the Klucher model [28]. For the ground diffuse part, the following formula was applied, assuming isotropic reflection with an albedo of 0.2 and a tilt angle β of 29° [29].

$$I_{ground-reflected} = \frac{1}{2} \cdot I_{global-horizontal} \cdot Albedo \cdot (1 - \cos(\beta)) \quad (2)$$

For sake of simplicity the same spectral distribution was assumed for the direct as well as the diffuse part of the spectrum for the following simulations as a first approximation.

4.4 Electrical solar cell parameters

The electrical simulation is based on two-diode models for the perovskite and the silicon solar cell. The respective parameters for the silicon solar cell were determined from fitting the light and dark IV-characteristic from a single-junction solar cell with 25.7% efficiency at STC [30], which resulted in: J_{01} = 2.282 •10^{-11} mA/cm^2, J_{02} = 7.663 • 10^{-7} mA/cm^2, R_P = 5000 Ωcm^2 and R_S = 0.1035 Ωcm^2. For the perovskite top cell, a published light IV-curve from a efficient perovskite solar cell with 22.7% STC-efficiency and a bandgap of 1.63 eV [31] was fitted using a two-diode model. The resulting saturation currents of J_{01} = 0 mA/cm^2 and J_{02} = 2.418 • 10^{-9} mA/cm^2, show that a single-diode model with an ideality factor of n = 2 is sufficient for modeling this specific cell. The extracted parallel and series resistances were R_P = 10000 Ωcm^2 and R_S = 1.221 Ωcm^2.

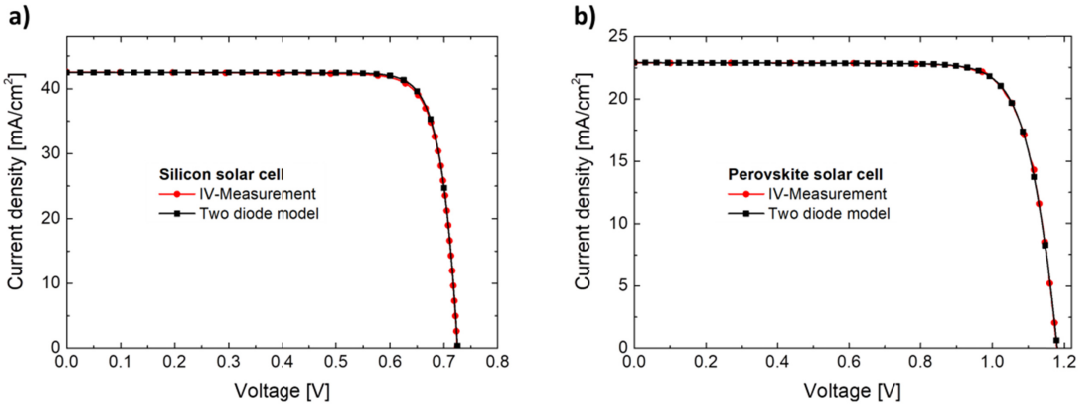

Fig. 4. Measured IV-characteristic of a silicon [30] (left) and a perovskite [31] single junction solar cell (right). Compared to the measured values are the fit curves of a two diode model for each of the cells.

Optics EXPRESS

The J_0 values for a bandgap of 1.7 eV were calculated assuming that the difference between bandgap energy and V_{oc} stays constant for different bandgaps. For the limited bandgap changes within this work this is a good approximation [32]. This consideration leads to $J_{02} = 6.225 \cdot 10^{-10}$ mA/cm^2 for the perovskite solar cell with a bandgap of 1.7 eV. Note that the series resistance of a solar cell mainly depends on the front and rear interfaces towards the contacts. Since only one of the two metal contacts of each subcell is relevant for a monolithic tandem device, the R_s-values of both subcells were divided in half for the energy yield calculation. This procedure leads to STC efficiencies of 25.9% and 27.7% for the modules featuring tandem cells with planar front and textured front, respectively. The single junction module shows an STC efficiency of 25.8%.

4.5 Energy yield analysis

All parameters described in the sections above are used as input for YieldOpt 2.0, which performs the energy yield analysis. The direct and diffuse incident spectra are multiplied with the EQE of the respective incidence angle and integrated to the short circuit current at every time step. Note that for the diffuse irradiance, the EQE of 55° incidence is applied [33]. Subsequently, the electrical parameters are used to calculate IV-characteristic, the maximum power point, the efficiency as well as the power output. Note that effects of varying temperature influence both the optical as well as the electrical cell performance but are not taken into account here. We focus on the effect of the texturing, different angles of incidence and different spectral conditions and assume a constant temperature of 25°C.

Figure 5(a) shows hourly data of the global irradiance on a module with south orientation and a tilt angle of 29° with respect to the average photon energy (APE). The APE is defined in Eq. (3) and integrated within this work from 300 nm to 1200 nm.

$$APE = \frac{\int I(\lambda)\, d\lambda}{\frac{q}{hc} \cdot \int I(\lambda) \cdot \lambda\, d\lambda} \tag{3}$$

The highest irradiance values appear during the summer months and correspond to average photon energies around 1.8 eV, which is also close to the APE of the AM1.5g spectrum [26]. This agrees well with the highest efficiencies, which are reached for the same APEs, as shown in Fig. 5(b) for the module with the front side textured solar cells. Note that the accuracy of irradiance measurement is relatively large for small irradiance values. For strongly distorted spectra with very low or very high APE, for which the efficiency of the perovskite silicon tandem solar cell drops, coincide with relatively low irradiance, thus the impact on the annual energy yield is low.

As reason for the drop in efficiency towards high and low APEs, an increased current mismatch for distorted spectra is assumed. Therefore, the current mismatch is analyzed in more detail. Figure 6(a) shows the relative current mismatch *RCM,* defined in Eq. (4), with respect to the global irradiance. *RCM* can be regarded as the current loss of the tandem device due to the current mismatch, $\frac{J_{top} - J_{bot}}{2}$, divided by the average of the currents, $\frac{J_{top} + J_{bot}}{2}$.

$$RCM = \frac{J_{top} - J_{bot}}{J_{top} + J_{bot}} \tag{4}$$

Optics EXPRESS

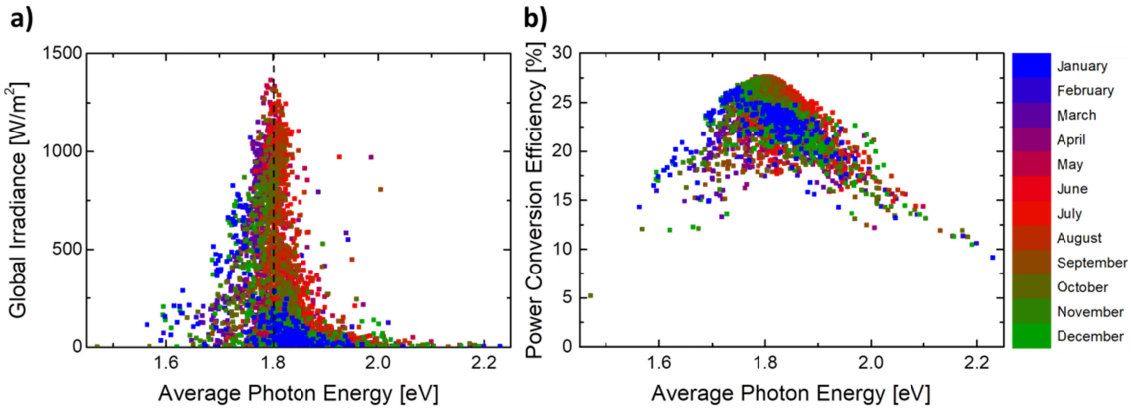

Fig. 5. (a) Distribution of the hourly global irradiance for Freiburg from February 2014 until January 2015. The dashed line indicates the APE of the AM1.5g spectrum [26]. (b) Distribution of the power conversion efficiency for a perovskite silicon tandem module with front side textured solar cells.

Figure 6(a) demonstrates that RCM values lower than −25% and larger than 25% are not uncommon. However, large deviations from the current matched situation occur again predominantly in combination with a low irradiance. Remarkably, weighting the relative current mismatch with the irradiance leads to a value of 2.8%, meaning that the device is on average limited by the bottom cell. This indicates further potential for optimizing the thin film stack, e.g. by using an average irradiance spectrum of the specific location during the layer stack optimization and not the AM1.5g standard spectrum.

Figure 6(b) shows the annual incident energy per square meter, which is added up for different intervals of the output power ratio between the module with front side textured tandem solar cells and the module with single junction silicon solar cell. The graph confirms clearly that tandem configuration is superior to the single junction case since the maximum of the output power ratio correlates strongly with high solar irradiance values.

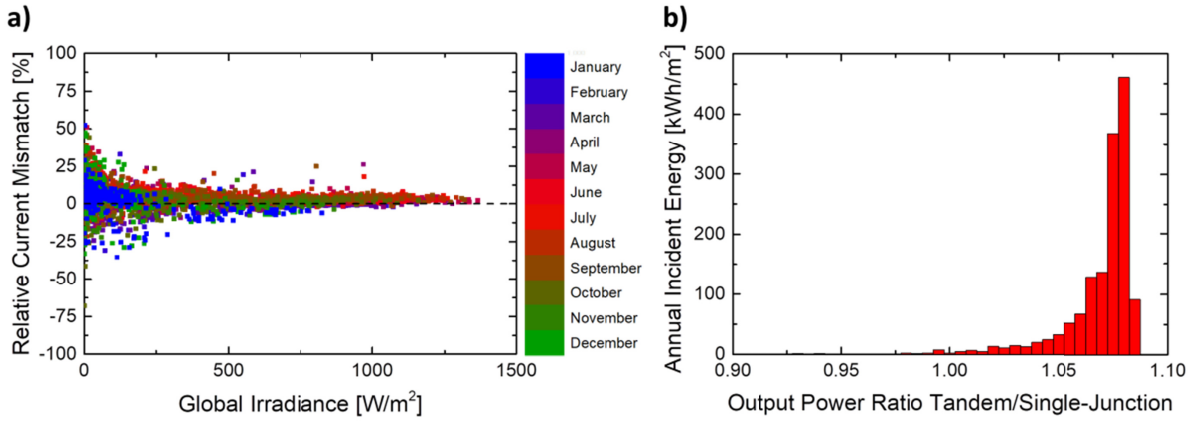

Fig. 6. (a) Relative current mismatch between perovskite top and silicon bottom cell with respect to the global incident power, for the module with the front side textured solar cells. (b) Annual incident energy for different output power ratios between the module with front side textured tandem cells and the one with single junction silicon cells.

The annual energy yield per square meter combines all of the analyses shown above into one single value. The results for the systems investigated in this work are collected in Table 3. The tandem module with the front side textured solar cells has the highest energy yield and

Optics EXPRESS

produces 7.3%$_{rel}$ more electricity than the module with silicon single junction solar cell (26% compared to 24.3% harvesting efficiency). For comparison, the efficiency under standard testing conditions was 7.8%$_{rel}$ higher. Hence, almost the complete efficiency advantage of the tandem device is translated into a higher energy yield, despite the current matching restriction of the monolithic tandem devices. Note that the fill factor of a tandem cell is low at current matching conditions and higher in mismatched situations. This is a very important effect for yield analyses of tandem solar cells as it reduces the power loss, which would be expected based on the mismatched current only.

The performance ratio, which is defined as the ratio between the annual energy yield and the efficiency multiplied by the annual incident energy, expresses the same trend. The module with the single junction silicon solar cells has the highest performance ratio of 94.2%, because it does not suffer from mismatch losses. However, the tandem module with textured front side solar cells features a value of 93.7%, which is very close.

The module with the front side textured tandem solar cells clearly outperforms the module with front side planar tandem solar cells, because of the strong reduction of reflection losses. Furthermore, it can make better use of irradiation at shallow angles, as the slightly larger difference between the harvesting efficiencies compared to the difference of the STC efficiencies shows. The module with planar front side tandem cells even shows a lower energy yield than the module with silicon single junction solar cells, despite its 0.1% higher efficiency under standard testing conditions.

Table 3. Energy yield and performance ratio for module stacks with different solar cells

	Perovskite silicon tandem (planar front)	Perovskite silicon tandem (textured front)	Silicon single junction
STC efficiency	25.9%	27.8%	25.8%
Annual incident energy [kWh/m^2]	1463	1463	1463
Energy yield [kWh/m^2]	347	381	355
Harvesting efficiency	23.7%	26.0%	24.3%
Performance ratio	91.6%	93.7%	94.2%

Despite the fact that realistic performance ratios in the field will be lower for all module types, as additional factors such as temperature, soiling, placement of the system and also losses in the power electronics will be relevant, this analysis demonstrates that solar modules with persovskite silicon tandem solar cells can outperform solar modules with single-junction high efficiency silicon solar cells. The comparable performance ratios of both module types highlight the energy yield potential of perovskite silicon tandem technology.

5. Conclusion and outlook

Simulation-based energy yield analyses for perovskite tandem solar cells and modules with textured interfaces can take realistic environmental conditions into account and therefore guide further developments. This work introduces a simulation scheme to calculate the energy yield including complex device configurations with surface structures as well as module encapsulation effects. The investigated perovskite silicon tandem modules with front side texture show a 7.3%$_{rel}$ higher energy yield compared to an encapsulated high efficiency silicon single junction cell for realistic irradiance conditions in Freiburg, Germany. This performance could be enhanced significantly by increasing the tandem efficiency, e.g. via less parasitic absorption in the charge transfer layers, especially the ITO. Furthermore, an optimization of the perovskite layer stack considering the irradiance of the specific location might lead to a reduction of the current mismatch and subsequently to a higher energy yield as well as performance ratio. A parameter that is not investigated within this work is the temperature. It influences the bandgap and thereby both the optical as well as the electrical device performance. Therefore, introducing realistic temperature dependence in a yield

analysis will be the subject of future work. Also possible performance difference due to different spectra for direct and diffuse irradiance need to be further investigated.

Funding

The German Research Foundation (DFG) in the project Oposit, the German Federal Ministry for Economic Affairs and Energy (0324037A), Persist and the EU project Sitasol (727497).

References

1. P. V. Oxford, "Oxford PV perovskite solar cell achieves 28% efficiency," https://www.solarnovus.com/oxford-pv-perovskite-solar-cell-achieves-28-efficiency_N11806.html (2018).
2. K. Yoshikawa, H. Kawasaki, W. Yoshida, T. Irie, K. Konishi, K. Nakano, T. Uto, D. Adachi, M. Kanematsu, H. Uzu, and K. Yamamoto, "Silicon heterojunction solar cell with interdigitated back contacts for a photoconversion efficiency over 26%," Nat. Energy **2**(5), 17032 (2017).
3. O. Dupré, B. Niesen, S. De Wolf, and C. Ballif, "Field Performance versus Standard Test Condition Efficiency of Tandem Solar Cells and the Singular Case of Perovskites/Silicon Devices," J. Phys. Chem. Lett. **9**(2), 446–458 (2018).
4. M. T. Hörantner and H. J. Snaith, "Predicting and optimising the energy yield of perovskite-on-silicon tandem solar cells under real world conditions," Energy Environ. Sci. **10**(9), 1983–1993 (2017).
5. I. Almansouri, A. Ho-Baillie, and M. A. Green, "Ultimate efficiency limit of single-junction perovskite and dual-junction perovskite/silicon two-terminal devices," Jpn. J. Appl. Phys. **54**(8S1), 08KD04 (2015).
6. N. N. Lal, T. P. White, and K. R. Catchpole, "Optics and Light Trapping for Tandem Solar Cells on Silicon," IEEE J. Photovoltaics **4**(6), 1380–1386 (2014).
7. P. Löper, S.-J. Moon, S. M. de Nicolas, B. Niesen, M. Ledinsky, S. Nicolay, J. Bailat, J.-H. Yum, S. De Wolf, and C. Ballif, "Organic-inorganic halide perovskite/crystalline silicon four-terminal tandem solar cells," Phys. Chem. Chem. Phys. **17**(3), 1619–1629 (2015).
8. M. Jošt, E. Köhnen, A. B. Morales-Vilches, B. Lipovšek, K. Jäger, B. Macco, A. Al-Ashouri, J. Krč, L. Korte, B. Rech, R. Schlatmann, M. Topič, B. Stannowski, and S. Albrecht, "Textured interfaces in monolithic perovskite/silicon tandem solar cells. Advanced light management for improved efficiency and energy yield," Energy Environ. Sci. **2**, 16196 (2018).
9. Y. Jiang, I. Almansouri, S. Huang, T. Young, Y. Li, Y. Peng, Q. Hou, L. Spiccia, U. Bach, Y.-B. Cheng, M. A. Green, and A. Ho-Baillie, "Optical analysis of perovskite/silicon tandem solar cells," J. Mater. Chem. C Mater. Opt. Electron. Devices **4**(24), 5679–5689 (2016).
10. M. van Eerden, M. Jaysankar, A. Hadipour, T. Merckx, J. J. Schermer, T. Aernouts, J. Poortmans, and U. W. Paetzold, "Optical Analysis of Planar Multicrystalline Perovskite Solar Cells," Adv. Opt. Mater. **5**(18), 1700151 (2017).
11. J. Lehr, M. Langenhorst, R. Schmager, S. Kirner, U. Lemmer, B. S. Richards, C. Case, and U. W. Paetzold, "Energy yield modelling of perovskite/silicon two-terminal tandem PV modules with flat and textured interfaces," Sustain. Energy Fuels **2**(12), 2754–2761 (2018).
12. M. A. Green, Y. Hishikawa, E. D. Dunlop, D. H. Levi, J. Hohl-Ebinger, and A. W. Y. Ho-Baillie, "Solar cell efficiency tables (version 52)," Prog. Photovolt. Res. Appl. **26**(7), 427–436 (2018).
13. Z. C. Holman, M. Filipič, A. Descoeudres, S. de Wolf, F. Smole, M. Topič, and C. Ballif, "Infrared light management in high-efficiency silicon heterojunction and rear-passivated solar cells," J. Appl. Phys. **113**(1), 13107 (2013).
14. A. J. Bett, P. S. C. Schulze, K. Winkler, J. Gasparetto, P. F. Ndione, M. Bivour, A. Hinsch, M. Kohlstädt, S. Lee, S. Mastroianni, L. E. Mundt, M. Mundus, C. Reichel, A. Richter, C. Veit, K. Wienands, U. Würfel, W. Veurman, S. W. Glunz, M. Hermle, and J. C. Goldschmidt, "Low temperature perovskite solar cells with an evaporated TiO 2 compact layer for perovskite silicon tandem solar cells," Energy Procedia **124**, 567–576 (2017).
15. S. L. Ren, Y. Wang, A. M. Rao, E. McRae, J. M. Holden, T. Hager, K. Wang, W.-T. Lee, H. F. Ni, J. Selegue, and P. C. Eklund, "Ellipsometric determination of the optical constants of C60 (Buckminsterfullerene) films," Appl. Phys. Lett. **59**(21), 2678–2680 (1991).
16. M. Filipič, P. Löper, B. Niesen, S. De Wolf, J. Krč, C. Ballif, and M. Topič, "CH(3)NH(3)PbI(3) perovskite / silicon tandem solar cells: characterization based optical simulations," Opt. Express **23**(7), A263–A278 (2015).
17. M. A. Green, "Self-consistent optical parameters of intrinsic silicon at 300 K including temperature coefficients," Sol. Energy Mater. Sol. Cells **92**(11), 1305–1310 (2008).
18. Y. Jiang, S. Pillai, and M. A. Green, "Realistic Silver Optical Constants for Plasmonics," Sci. Rep. **6**(1), 30605 (2016).
19. M. J. Dodge, "Refractive properties of magnesium fluoride," Appl. Opt. **23**(12), 1980 (1984).
20. K. R. McIntosh, J. N. Cotsell, A. W. Norris, N. E. Powell, and B. M. Ketola, "An optical comparison of silicone and EVA encapsulants under various spectra," in Proceedings of the 35th IEEE Photovoltaic Specialists Conference (PVSC) (IEEE, 2010), pp. 269–274.

Optics EXPRESS

21. S. Duttagupta, F. Ma, B. Hoex, T. Mueller, and A. G. Aberle, "Optimised Antireflection Coatings using Silicon Nitride on Textured Silicon Surfaces based on Measurements and Multidimensional Modelling," Energy Procedia **15**, 78–83 (2012).
22. N. Tucher, O. Höhn, J. C. Goldschmidt, and B. Bläsi, "Optical modeling of structured silicon-based tandem solar cells and module stacks," Opt. Express **26**(18), A761–A768 (2018).
23. N. Tucher, J. Eisenlohr, P. Kiefel, O. Höhn, H. Hauser, M. Peters, C. Müller, J. C. Goldschmidt, and B. Bläsi, "3D optical simulation formalism OPTOS for textured silicon solar cells," Opt. Express **23**(24), A1720–A1734 (2015).
24. C. Gueymard, *SMARTS2, A Simple Model of the Atmospheric Radiative Transfer of Sunshine*, (Florida Solar Energy Center, 1995).
25. M. Steiner, G. Siefer, T. Hornung, G. Peharz, and A. W. Bett, "YieldOpt, a model to predict the power output and energy yield for concentrating photovoltaic modules," Prog. Photovolt. Res. Appl. **23**(3), 385–397 (2015).
26. IEC, *Photovoltaic Devices - Part 3. Measurement Principles for Terrestrial Photovoltaic (PV) Solar Devices with Reference Spectral Irradiance Data* (International Electrotechnical Commission, 2008), 2nd edition.
27. P. Löper, M. Stuckelberger, B. Niesen, J. Werner, M. Filipič, S.-J. Moon, J.-H. Yum, M. Topič, S. De Wolf, and C. Ballif, "Complex Refractive Index Spectra of CH3NH3PbI3 Perovskite Thin Films Determined by Spectroscopic Ellipsometry and Spectrophotometry," J. Phys. Chem. Lett. **6**(1), 66–71 (2015).
28. T. M. Klucher, "Evaluation of models to predict insolation on tilted surfaces," Sol. Energy **23**(2), 111–114 (1979).
29. P. G. Loutzenhiser, H. Manz, C. Felsmann, P. A. Strachan, T. Frank, and G. M. Maxwell, "Empirical validation of models to compute solar irradiance on inclined surfaces for building energy simulation," Sol. Energy **81**(2), 254–267 (2007).
30. A. Richter, J. Benick, F. Feldmann, A. Fell, M. Hermle, and S. W. Glunz, "n-Type Si solar cells with passivating electron contact. Identifying sources for efficiency limitations by wafer thickness and resistivity variation," Sol. Energy Mater. Sol. Cells **173**, 96–105 (2017).
31. M. Saliba, T. Matsui, K. Domanski, J.-Y. Seo, A. Ummadisingu, S. M. Zakeeruddin, J.-P. Correa-Baena, W. R. Tress, A. Abate, A. Hagfeldt, and M. Grätzel, "Incorporation of rubidium cations into perovskite solar cells improves photovoltaic performance," Science **354**(6309), 206–209 (2016).
32. R. R. King, D. Bhusari, A. Boca, D. Larrabee, X.-Q. Liu, W. Hong, C. M. Fetzer, D. C. Law, and N. H. Karam, "Band gap-voltage offset and energy production in next-generation multijunction solar cells," Prog. Photovolt. Res. Appl. **19**(7), 797–812 (2011).
33. D. Dirnberger, B. Müller, and C. Reise, "PV module energy rating. Opportunities and limitations," Prog. Photovolt. Res. Appl. **23**(12), 1754–1770 (2015).